Electrically Suppressed Outflow of Confined Liquid in Hydrophobic Nanopores

Yuan Gao[1], Mengtian Yin[1], Haozhe Zhang[1], and Baoxing Xu[1,*]

[1]Department of Mechanical and Aerospace Engineering, University of Virginia,
Charlottesville, VA 22904, USA

[*]Corresponding author. bx4c@virginia.edu

Abstract

Confining liquid in a hydrophobic nanoenvironment has enabled a broad spectrum of applications in biomedical sensors, mechanical actuators, and energy storage and converters, where the outflow of confined liquid is spontaneous and fast due to the intrinsic hydrophobic nature of nanopores with extremely low interfacial friction, challenging design capacity and control tolerance of structures and devices. Here, we present a facile approach of suppressing the outflow of water confined in hydrophobic nanopores with an electric field. Extensive molecular dynamics simulations show that the presence of an electric field could significantly strengthen hydrogen bonds and retards degradations of the associated networks during the outflow. The outflow deformation and strength are extracted to quantitatively characterize the electrical suppression to outflow and agree well with simulations. This study proposes a practical means of impeding the fast liquid outflow in hydrophobic nanopores, potentially useful for devising nanofluidics-based functional structures and devices with controllable performance.

Keywords: *nanofluidics, hydrophobic nanopores, outflow, electric field, hydrogen bonding network.*

Introduction

Liquids confined in hydrophobic nanopores and nanochannels have demonstrated extraordinary electrical, transport, and hydrodynamic properties due to strong nanoconfinement effects, including superfluidity,[1-3] fast mass transport,[4-8] anomalously low and negative dielectric constants,[9-11] Coulomb blockade,[12] solid-like ordering,[13] enhanced thermal transport,[14, 15] and extreme phase transition temperature.[16, 17] These unconventional properties have enabled numerous designs and explorations to nanofluidics-based functional structures and devices with broad applications in chemical and biological sensing,[18-20] energy storage and conversion,[21-23] fluidic transistors and diodes,[24, 25] mechanical absorbers/dissipaters and actuators,[26, 27] and water desalination.[28-30] Among these designs, because of the hydrophobic nature of nanopores and nanochannels that will drive the spontaneous, fast outflow of liquids once intruded, the regulation and control of the outflow is the key. For example, slowing down the translocation speeds of liquid molecules flowing out of solid-state nanopores is essential to improve the sensitivity of biosensing.[31] Outflow control to the intruded liquid is also the foundation in nanoporous materials-liquid-enabled reusable energy dissipation systems.[32, 33] Moreover, with the appropriate control and manipulation of confined liquid outflow, the release of associated solid-liquid interfacial energy can lead to a significant mechanical output/strain and has been leveraged to design nanofluidics-based actuators.[34]

In fundamental, the intrusion process of bulk liquid into hydrophobic nanopores is a continuous and stable stage even subjected to an external stimulus such as electric field[35, 36] or temperature.[37] By contrast, the outflow of confined liquid usually shows a metastable state due to the enhanced cohesion of liquid molecules at a confined nanoenvironment,[38, 39] which hinders the outflow. Besides, our recent work reveals that this liquid outflow is intimately determined by dynamic orientations of molecular dipoles and hydrogen-bond networks at the liquid-nanopore interface and can be well described by a solid-like mechanics model with the incorporation of temperature and pore size.[40] Inspired by the response of solid-liquid interaction to electric fields, harnessing the solid-like outflow behavior and the associated metastable state of liquid confinements in an electric field could yield a promising manipulation strategy and control approach to liquid outflow, but is currently lacking. In this work, we report an electrical suppression approach to slow down the outflow of water confined in hydrophobic nanopores. Full-scale molecular dynamics (MD) simulations were performed, and the results show that the presence of an electric field across the nanopores could significantly weaken and even break the cohesion of confined water molecules in nanopores, thus retarding the outflow process. Further comprehensive analyses on the internal stress and hydrogen bonding (H-bond) network of the confined water suggest the electric field enhance largely the arrangement order of the H-bond networks and thus alleviate degradation of H-bond networks during outflow. Besides, the rotational dynamics of water molecules is restricted by an electric field, which agrees well with the suppressed outflow of confined water. The present study suggests a facile approach to slow down the fast outflow of confined liquid with electric fields and could be used for designing electrically controllable nanofluidic devices and functional structures.

Results and Discussion

Retardation in outflow of intruded liquid under an electric field. The inset of **Figure 1a** depicts the atomistic modeling, which includes a hydrophobic silica nanotube with a length of $L_0 = 11.95$ nm and a variable radius r_0 fully immersed in a water reservoir. The reservoir is sandwiched between a rigid piston (positive z-direction) and a rigid wall (negative z-direction). Details of the modeling are included in the Methods section. Figure 1a presents the history of the pressure P exerted on the piston during a loading-unloading cycle, equivalent to the hydrostatic pressure in the hydrophobic nanopore/water system, where the radius of nanopore

r_0 is 1.57 nm. In the absence of a pressure loading, water molecules cannot spontaneously infiltrate the nanopore due to its hydrophobic nature. Upon a quasistatic pressure loading, P initially increases with the system volume change $\Delta V/V_0$ (black curve), where V_0 denotes the initial volume of the system. A plateau of P is observed as it reaches the infiltration pressure $P_{\mathrm{in}} = 63.2$ MPa (determined as the plateau value), where the water molecules substantially infiltrate the nanopore at the overcoming of capillary resistance. With $\Delta V/V_0 = 0.083$, a confined water cylinder is formed and fully occupies the nanopore, leading to the incompressibility of the system and the following rapid increase in P with $\Delta V/V_0$.

During the quasistatic unloading process, the solid-liquid interaction drives the outflow, leading to the reduction in P. The P-$\Delta V/V_0$ relation coincides with the loading history before the system recovers from the overloading stage with $\Delta V/V_0 > 0.083$ (colorful curves). The P history starts to deviate from that during the loading, and the deviation $(P_{\mathrm{in}} - P)$ reflects the confined liquid cohesion against the outflow. Based on the pressure balance in the system, the outflow can be modeled as a uniaxial tensile load on the confined water cylinder.[40] A nominal stress σ and strain ε can be defined as $(P_{\mathrm{in}} - P)$ and $(\Delta V_{\mathrm{its}}/V_0 - \Delta V/V_0)$, respectively, to characterize the outflow (**Figure 1b**), where ΔV_{its} is the critical volume change that leads to the complete infiltration of the nanopore.[40] The turning point in the P-$\Delta V/V_0$ curve indicates the breakdown of liquid cohesion and the failure of the confined water cylinder, which corresponds to the ultimate stress in the σ-ε curve. The P-$\Delta V/V_0$ relationship returns to that during the loading process after the breakdown of liquid cohesion, which triggers substantial outflow reflected by the rapid reduction in the number of confined water molecules N_{w} (**Figure 1c**). Such a triggering mechanism is different from that due to the variation in confinement geometry.[41, 42] In the presence of an electric field in the positive z-direction, the substantial outflow is delayed, as reflected by a higher ultimate stress and failure strain in Figure 1b. **Video**

S1 presents the atomistic animation showing the retardation of outflow in the presence of an electric field. With an enhanced strength of electric field E, the delay is more significant. However, the applied electric field does not influence the early stage of outflow before the failure of the confined water, suggested by the similar slopes in σ-ε and N_{w}-ε curves. Similar phenomena can be observed with different confinement sizes r_0 (see **Figures S1 and S2**). Further analyses indicate that the applied electric field does not introduce asymmetric outflow before the break of the confined water cylinder (**Figure S3**).

Figure. 1d,e presents a series of snapshots of the confined water molecules during the outflow process with $E = 0$ and 0.3 V/nm. The shapes of the water cylinders are almost the same when $\varepsilon \leq 4.0\%$ despite the presence of the electric field. The solid-like necking behavior is delayed with $E = 0.3$ V/nm at $\varepsilon = 6.8\%$, compared to $\varepsilon = 5.3\%$ without electric fields. **Figure 1f,g** shows the evolution of confined molecule number $N_{\mathrm{w,local}}$ at various radial locations r/r_0 and nominal strain ε values, normalized by its maximum, confirming that the applied electric field can delay the outflow. For both $E = 0$ and 0.3 V/nm, the outflow occurs adjacent to the nanopore wall, reflected by the "yellow notch" $r/r_0 = 0.8$.

Mechanical characterization of the outflow. Extensive calculations are performed to investigate the effects of confinement size r_0 and electric field strength E on the outflow. The outflow is quantitatively characterized by the elastic modulus Y and ultimate stress F_{TU} of the confined water cylinder (see Methods section), corresponding to the early and later stages of the outflow. According to **Figure 2a**, Y does not depend on the electric field. In contrast, F_{TU} increases with the increase of E. Both Y and F_{TU} show enhancements at a stronger confinement effect (smaller r_0). These observations can be further understood by examining the polar structures of confined water molecules via the polar structural factor $S(\boldsymbol{q})$ (see Methods section).

Figure 2c shows that a regular, rotational-symmetric scattering pattern in $S(\boldsymbol{q})$ is observed with $E = 0$ V/nm and $\varepsilon = 0\%$, indicating the ordered intermolecular structure of water molecules due to the confinement effect. An electric field with $E = 0.3$ V/nm does not impact the pattern or the intermolecular structure, corresponding to an unchanged Y. A similar phenomenon is observed with different confinement sizes r_0 (**Figure S4**). With $E = 0$ V/nm and $\varepsilon = 5\%$, the intensity at $|\boldsymbol{q}| = 0.5$ nm^{-1} vanishes, suggesting the loss of molecules adjacent to the solid-liquid interface due to the outflow. In addition, the dot-like patterns at $|\boldsymbol{q}| = 0.25$ nm^{-1} become discontinuous rings, indicating that the intermolecular structure becomes disordered. However, the electric field $E = 0.3$ V/nm can maintain the dot-like patterns and the structural order at $\varepsilon = 5\%$.

Degradation of hydrogen-bonding network. Analyses on the H-bond network are carried out to understand the outflow mechanism subject to an electric field. **Figure 3a** demonstrates the H-bond snapshots, where the balls and sticks represent water molecules and H-bonds, respectively, and the color indicates the number of H-bonds owned by a water molecule n_{HB}. At $\varepsilon = 0\%$, the H-bonds network spread over the water cylinder, and n_{HB} is higher near the central axis for both $E = 0$ and 0.3 V/nm. Close to failure of the water cylinder ($\varepsilon = 5.3\%$ and 6.8% for $E = 0$ and 0.3 V/nm), the H-bond network is reduced to one or several chains within the necking region while the rest of the network remains unchanged, suggesting that the network degradation is a localized effect (**Video S2**). **Figure 3b** illustrates the evolution of the ensemble average of the H-bond occupation $< n_{\mathrm{HB}} >$ during the outflow with various E. A higher E can delay the reduction in $< n_{\mathrm{HB}} >$, which is consistent with the delay in N_{w} (Figure 1c). In addition, such reduction is more significant after the failure of the confined water (marked by the '×' symbols) but remains almost constant beforehand, which confirms the localized feature in H-bond-network degradation. The same statement can be drawn by comparing the evolution of $< n_{\mathrm{HB}} >$ within the necking region according to the inset of Figure 3b. These localized features under electric fields are different from that in the electrowetting of hydrophobic membranes and channels.[43, 44]

To further probe the H-bond degradation, **Figure. 3c,d** demonstrates the variation of local H-bond number density ρ_{HB} with ε at different radial locations r/r_0. The black dashed line separates the bulk region and interface region, where the interface region is recognized by the outermost peak in the radial number density distribution (**Figure S5**). A significant ρ_{HB} peak locates in the interface layer for both $E = 0$ and 0.3 V/nm, which is caused by the densification of water molecules.[40] The higher ρ_{HB} is correlated with the notable surface stress exerted on the confined water, presented in **Figure 3e,f**. During the outflow, such peak is reduced by the loss of molecules and vanishes before the failure of the water cylinder, illustrating the H-bond degradation is initiated in the interface layer. In addition, the outflow leads to a blurred pattern in the distribution of ρ_{HB} in the bulk region, suggesting a more disordered intermolecular structure at a higher ε, which is also reflected by the wavy radial distribution in axial virial stress σ_{zz} at $\varepsilon = 5\%$ in Figure 3e. With $E = 0.3$ V/nm, this effect of structural disorder is suppressed, as presented in Figure 3d,f. This suppression agrees with the enhanced surface stress and the increase of the associated surface energy density by the electric field (**Figures S6 and S7**), which is similar to the electrowetting of hydrophobic membranes and channels.[43, 44] **Figure 3g** shows the ensemble average of the H-bond orientation $< \cos(\theta_{\mathrm{HB}-z}) >$, where $\theta_{\mathrm{HB}-z}$ is the angle formed by the nanopore axis and H-bonds and ranges between 0 and 90 degrees. The insets present the $\cos(\theta_{\mathrm{HB}-z})$ contours with axial and radial locations at $\varepsilon = 0$ (left) and 5% (right), and with $E = 0$ (top) and 0.3 V/nm (bottom). Variations of tetrahedral order parameter further confirms the change of intermolecular structures during the outflow (**Figure S8**).

Mechanisms in dynamics of confined molecules. Figure 4 compares the H-bond potential of mean force (PMF, see Methods section) with respect to the molecular separation $r_{\rm OO}$ and pair angle $\theta_{\rm OH}$ (inset of Figure 4a) with different ε and E. Each pair of water molecules with potential of forming an H-bond is considered. The rectangular region at the bottom-left corresponds to the formation of H-bonds, and a lower PMF in this region suggests a higher H-bond strength.[45] Two PMF barriers (in red color) locate at the top and on the right of the H-bond region, and respectively correspond to breaking an H-bond with the rotational and translational motion of water molecules. A saddle region locates around $r_{\rm OO}$ = 3.2 Å and $\theta_{\rm OH}$ = 35 degrees. Without the applied electric field, the outflow reduces the strength of H-bonds at $\varepsilon = 5\%$, demonstrated by the broadened saddle and the lowered PMF in the valley outside the H-bond region (Figure 4b). In the presence of an electric field with $E = 0.3$ V/nm, the PMF remains the same as that in the absence of the electric field at $\varepsilon = 0$ (Figure 4c), in good consistency with the unchanged intermolecular structure in Figure 3b,g. However, the electric field can maintain the H-bond strength against the outflow at $\varepsilon = 5\%$, indicated by a similar PMF contour at $\varepsilon = 0\%$ (Figure 4d).

To understand the molecular mechanisms of the H-bond orientation (Figure 3g), **Figure 5a** shows the probability density distribution of the angle between the axial (z-) direction dipole orientation $\theta_{\mu-z}$ at various radial locations r/r_0 ($r_0 = 1.57$ nm) with $\varepsilon = 0\%$. The distributions are different in bulk and interface regions. The dominance of $\theta_{\mu-z}$ is 90 degrees in the bulk region, while two preferences locate at 45 and 135 degrees in the interface layer, which are caused by the solid-liquid interaction. In general, the distribution is axial-symmetric with respect to $\theta_{\mu-z} = 90$ degrees. With $E = 0.3$ V/nm **(Figure 5b)**, the symmetry of the distribution breaks down and the preference of $\theta_{\mu-z}$ shifts to ~ 135 degrees, indicating the strong regulation effect on water orientation. We should note that this dipole behavior may lead to a local variation of the applied static electric field.[46] **Figure 5c** further shows the probability density distribution of $\theta_{\mu-z}$ with $E = 0$ and smaller nanopore size ($r_0 =$ 1.07 nm). Consequently, a higher portion of confined water molecules is included in the interface region as the border shifts to $r/r_0 = 0.4$ (Figure S5). However, the preference of $\theta_{\mu-z}$ in bulk and interface regions remains the same as that with $r_0 =$ 1.57 nm (Figure 5a). The electric field of $E = 0.3$ V/nm generates a similar impact on $\theta_{\mu-z}$, as shown in **Figure 5d**.

Both rotational and translational dynamics of the confined water that reflects structural rearrangement were also extracted to understand the molecular mechanisms in the retardation of H-bond-network degradation subject to an electric field. **Figure 5e** plots the effect of the electric field on the rotational dynamics of the confined water, where the rotational correlation time τ_{rot} is determined by fitting the rotational auto-correlation function $C_\mu(\tau)$ (see Methods section and **Figure S9**). In the absence of the electric field, at $\varepsilon = 0\%$, τ_{rot} is ~1.25 ps at different radial locations r/r_0 (solid navy symbols), close to that in water without confinement (dashed cyan line). At $\varepsilon = 5\%$, τ_{rot} slightly drops to ~1.20 ps within the interface region, suggesting more vibrant rotational dynamics (hollow navy symbols), which corresponds to the degradation of H-bond initiated in the interface region (Figure 3c). An electric field with $E =$ 0.3 V/nm systematically promotes τ_{rot} above 1.6 ps at $\varepsilon = 0\%$ (solid red symbols), which indicates the restriction on the rotational dynamics of the confined water molecules and corresponds to the delay in the H-bond-network degradation (Figure 3d). In addition, τ_{rot} within the interface region increases to ~1.75 ps, notably higher than 1.60 ps obtained without confinement (pink dashed curve). This phenomenon suggests that the electric field can enhance the confinement effect and further restrict the rotational dynamics close to the solid-liquid interface. At $\varepsilon = 5\%$, τ_{rot} drops to 1.60 ps (hollow red symbols), similar to the case without electric fields.

To highlight the effect of confinement size on the rotational dynamics of water molecules, **Figure 5f** shows τ_{rot} in nanopores with $r_0 = 1.07$ and 1.31 nm at $\varepsilon = 0\%$. In the absence of electric fields, τ_{rot} with $r_0 = 1.31$ nm (solid navy symbols) and 1.07 nm (hollow navy symbols) is close to that with $r_0 = 1.57$ nm. However, the electric field with $E = 0.3$ V/nm can further enhance τ_{rot} if the confinement effect is stronger (*i.e.*, smaller r_0), indicating more severe restrictions on the rotational dynamics, which is consistent with the higher ultimate stress F_{TU} at a smaller r_0 in Figure 2b. In addition, analyses of the mean square displacement indicate that the electric field can restrict the translational dynamics of confined water molecules (see **Figures S10 and S11**), which also partially contributes to the delay of outflow.

Conclusion

We have reported the outflow suppression of confined water in a hydrophobic nanopore with an electric field. Full-scale MD simulations were performed, and the results indicate that once the liquid is intruded into a hydrophobic nanopore, the subsequent outflow process is composed of an initial continuous part and a substantial one associated with the failure of the confined water. The electric field could enhance the ultimate failure strength of the confined water, leading to an overall delay in the outflow process. Extensive calculations also reveal that the presence of an electric field promotes the arrangement order of the H-bond network and thus delays its degradation. Further study on the intermolecular structural rearrangement indicates that this alleviated degradation attributes to the restriction to the rotational dynamics of confined water molecules. Besides, smaller confinement pore sizes lead to more severe restrictions. The present study offers a mechanism foundation for understanding the outflow of confined liquid in response to an external electric field and also sheds insights for electrically controlling and manipulating the confined liquid in the design of nanofluidic devices and functional structures.

Methods

Atomistic modeling and computational methods. The computational model contained a hydrophobic silica nanotube with a length of $L_0 = 11.95$ nm and a radius $r_0 = 1.07$, 1.31, or 1.57 nm immersed in a water reservoir. The water reservoir possessed a dimension of 7 nm (x-direction) × 7 nm (y-direction) × 20 nm (z-direction) and was sandwiched by a piston moving in the z-direction, and a rigid wall. The upper and lower ends were separated by ~6 and ~2 nm from the piston (positive z) and wall (negative z), respectively. The behavior of water molecules were described by the SPC/E model[47] while the silica nanotube were considered as rigid as its rigidity does not affect the outflow behavior.[40] The interaction between the nanotube and water molecules were modeled by the Lennard-Jones potential.[33] To mimic the hydrophobicity of the nanopore, the equilibrium distance and potential well depth of the solid-liquid interaction were set as $\sigma_{\mathrm{O,water-Si,nanopore}} = 3.319$ Å, $\varepsilon_{\mathrm{O,water-Si,nanopore}} = 0.1423$ kcal/mol, $\sigma_{\mathrm{O,water-O,nanopore}} = 3.319$ Å, and $\varepsilon_{\mathrm{O,water-O,nanopore}} = 0.0455$ kcal/mol.[48] The particle-particle-particle-mesh (PPPM) method with a root mean of 0.0001 was applied to evaluate the long range Coulombic interactions. Periodic boundary conditions were applied to both x and y-directions.

All molecular dynamics simulations were performed with LAMMPS.[49] The timestep was set as 1 fs. The system was first equilibrated in the canonical (NVT) ensemble at the temperature $T = 300$ K for 1 ns. In the following 1ns, the location of the piston was slightly adjusted with a rigid body algorithm[50] to ensure a zero pressure P on the piston. Next, A quasistatic displacement load in the negative z-direction was applied on the piston to intrigue the infiltration of water molecules. After the completion of infiltration, the system became incompressible. An electric with a strength E between 0 and 0.3 V/nm, on the same order of that in ion channels or membranes,[51, 52] was applied in the positive z-direction across the nanotube. Such method has proved well in the study of the electrical effects on confined liquids.[53, 54] Meanwhile, a quasistatic displacement in the positive z-direction was applied on the piston to perform unloading, which initiated the outflow of confined water molecules.

Mechanical characterization method. The elastic modulus E was determine by taking the linear stage of the nominal stress (σ)-strain (ε) relationship within $\varepsilon \leq 3\%$. The ultimate stress F_{TU} was taken as the maximum of σ, averaged by the values in the adjacent 10 ps. To reduce the error caused by the thermodynamic noise,[55] each simulation was repeated by 5 times with different random initial velocities of each atom, and the averaged results of Y and F_{TU} were reported in Figure 2.

Structural factor. The structural factor $S(\boldsymbol{q})$ was calculated as[17]

$$S(\boldsymbol{q}) = \langle \frac{1}{N_{\mathrm{w}}} \left[\left(\sum_{i=1}^{N_{\mathrm{w}}} \cos(\boldsymbol{q} \cdot \boldsymbol{r}_i) \right)^2 + \left(\sum_{i=1}^{N_{\mathrm{w}}} \sin(\boldsymbol{q} \cdot \boldsymbol{r}_i) \right)^2 \right] \rangle. \qquad (1)$$

In this expression,$\boldsymbol{q}$ represents the scattering vector, $\boldsymbol{r_i}$ is the position vector of the i-th oxygen atom confined in the nanotube, N_{w} is the total number of confined water molecules, and the bracket denotes the ensemble average. At least 10,000 frames of molecular coordinates during 0.5 ns were utilized to obtain the $S(\boldsymbol{q})$ at a given nominal strain ε and electric field strength E.

Potential of mean force. The potential of mean force PMF with respect to the molecular separation r_{OO} and pair angle θ_{OH} were determined by PMF $= -k_B T g(r_{\mathrm{OO}}, \theta_{\mathrm{OH}})$,[45] where k_B is the Boltzmann constant and T is the temperature. The distribution function of the two variables $g(r_{\mathrm{OO}}, \theta_{\mathrm{OH}})$ was defined as the ratio of the average number of oxygen atoms in a shell between r_{OO} and $r_{\mathrm{OO}} + dr_{\mathrm{OO}}$ from a specific O atom if the pair angle θ_{OH} is between $\theta_{\mathrm{OH}} + d\theta_{\mathrm{OH}}$, to the same number if the molecules were noninteracting, which is $2\pi\rho_{\mathrm{c}} \sin\theta_{\mathrm{OH}}\, d\theta_{\mathrm{OH}} r_{\mathrm{OO}}^2 dr_{\mathrm{OO}}$. Here, ρ_{c} is the number density of the confined water. In our calculations, the steps for radius $d\theta_{\mathrm{OH}}$ and angles θ_{OH} were 0.01 Å and 0.4 degrees, respectively. At least 10,000 frames of molecular coordinates during 0.5 ns were utilized to obtain the PMF at a given nominal strain ε and electric field strength E.

Rotational and translational dynamics. The rotational dynamics of the confined water molecules was investigated with the rotational auto-correlation function coupled with the 2nd-order Lagrange Polynomials[56]

$$C_{\mu}(\tau) = \frac{1}{2} < 3[\boldsymbol{\mu}(t) \cdot \boldsymbol{\mu}(t+\tau)]^2 - 1 >_t, \tag{2}$$

where $\boldsymbol{\mu}$ is the dipole vector at time t. The rotational correlation time τ_{rot} can be obtained by fitting the decay of $C_{\mu}(\tau)$ to an exponential function

$$C_{\mu}(\tau) \propto \exp\left(-\frac{\tau}{\tau_{\mathrm{rot}}}\right). \tag{3}$$

The translational dynamics of the confined water molecules was discussed with the mean-square displacement, MSD, calculated via

$$\mathrm{MSD}(\tau) =< |\boldsymbol{r}_i(t+\tau) - \boldsymbol{r}_i(t)|^2 >. \tag{4}$$

The virial stress was calculated via

$$\sigma_{ij} = \frac{1}{V_{\mathrm{slab}}} \sum_{k}^{N_{\mathrm{slab}}} (m_k v_{k,i} v_{k,j} + r_{k,i} f_{k,j}), \tag{5}$$

where V_{slab} is the volume of the slab, subscript k denotes the k-th atom in the slab, m_k is the atomic mass, $v_{k,i}$ and $v_{k,j}$ are the atomic velocity vector components in the i and j-directions, respectively, $r_{k,i}$ is the position vector component in the i-direction, and $f_{k,j}$ denotes the force vector component in the j-direction.

Supporting Information

Supporting Figures S1-11 showing additional pressure loading curves; nominal stress-strain curves; outflow rates at both ends of nanotubes; polar structural factor; radial number density distribution; confinement stress distribution; tetrahedral order parameter; rotational correlation function; mean-square displacement (PDF). Supporting Video S1 showing the molecular animation of confined water molecules during the outflow with an applied electric field. Supporting Video S2 showing the degradation of hydrogen-bonding network during the outflow with an applied electric field.

Author Contributions

Y.G. and B.X. conceived the studies. Y.G. performed the research. Y.G., M.Y., and H.Z. analyzed data. Y.G and B.X. wrote the manuscript.

Notes

The authors declare no conflicts of interest.

Acknowledgments

B.X. acknowledges the National Science Foundation Directorate for Engineering Division of Chemical, Bioengineering, Environmental and Transport Systems (Grant #1805451). This work in part used the Extreme Science and Engineering Discovery Environment (XSEDE) through allocation TG-MCH210002, which is supported by the National Science Foundation (grant number ACI-1548562).

References

(1) Chen, L.; Tu, B.; Lu, X.; Li, F.; Jiang, L.; Antonietti, M.; Xiao, K. Unidirectional Ion Transport in Nanoporous Carbon Membranes with a Hierarchical Pore Architecture. *Nat. Commun.* **2021,** *12*, 1-7.

(2) Tunuguntla, R. H.; Henley, R. Y.; Yao, Y.-C.; Pham, T. A.; Wanunu, M.; Noy, A. Enhanced Water Permeability and Tunable Ion Selectivity in Subnanometer Carbon Nanotube Porins. *Science* **2017,** *357*,

792-796.

(3) Secchi, E.; Marbach, S.; Niguès, A.; Stein, D.; Siria, A.; Bocquet, L. Massive Radius-Dependent Flow Slippage in Carbon Nanotubes. *Nature* **2016,** *537*, 210-213.

(4) Bocquet, L.; Charlaix, E. Nanofluidics, from Bulk to Interfaces. *Chem. Soc. Rev* **2010,** *39*, 1073-1095.

(5) Holt, J. K.; Park, H. G.; Wang, Y.; Stadermann, M.; Artyukhin, A. B.; Grigoropoulos, C. P.; Noy, A.; Bakajin, O. Fast Mass Transport through Sub-2-Nanometer Carbon Nanotubes. *Science* **2006,** *312*, 1034-1037.

(6) Abraham, J.; Vasu, K. S.; Williams, C. D.; Gopinadhan, K.; Su, Y.; Cherian, C. T.; Dix, J.; Prestat, E.; Haigh, S. J.; Grigorieva, I. V. Tunable Sieving of Ions Using Graphene Oxide Membranes. *Nat. Nanotechnol.* **2017,** *12*, 546-550.

(7) Falk, K.; Sedlmeier, F.; Joly, L.; Netz, R. R.; Bocquet, L. Molecular Origin of Fast Water Transport in Carbon Nanotube Membranes: Superlubricity Versus Curvature Dependent Friction. *Nano Lett.* **2010,** *10*, 4067-4073.

(8) Wang, X.; Liu, M.; Jing, D.; Mohamad, A.; Prezhdo, O. Net Unidirectional Fluid Transport in Locally Heated Nanochannel by Thermo-Osmosis. *Nano Lett.* **2020,** *20*, 8965-8971.

(9) Fumagalli, L.; Esfandiar, A.; Fabregas, R.; Hu, S.; Ares, P.; Janardanan, A.; Yang, Q.; Radha, B.; Taniguchi, T.; Watanabe, K. Anomalously Low Dielectric Constant of Confined Water. *Science* **2018,** *360*, 1339-1342.

(10) Sugahara, A.; Ando, Y.; Kajiyama, S.; Yazawa, K.; Gotoh, K.; Otani, M.; Okubo, M.; Yamada, A. Negative Dielectric Constant of Water Confined in Nanosheets. *Nat. Comm.* **2019,** *10*, 1-7.

(11) Schlaich, A.; Knapp, E. W.; Netz, R. R. Water Dielectric Effects in Planar Confinement. *Phys. Rev. Lett.* **2016,** *117*, 048001.

(12) Feng, J.; Liu, K.; Graf, M.; Dumcenco, D.; Kis, A.; Di Ventra, M.; Radenovic, A. Observation of Ionic Coulomb Blockade in Nanopores. *Nat. Mater.* **2016,** *15*, 850-855.

(13) Chakraborty, S.; Kumar, H.; Dasgupta, C.; Maiti, P. K. Confined Water: Structure, Dynamics, and Thermodynamics. *Acc. Chem. Res.* **2017,** *50*, 2139-2146.

(14) Wen, D. Mechanisms of Thermal Nanofluids on Enhanced Critical Heat Flux (Chf). *Int. J. Heat Mass Transfer* **2008,** *51*, 4958-4965.

(15) Matin, M. H. Electroviscous Effects on Thermal Transport of Electrolytes in Pressure Driven Flow through Nanoslit. *Int. J. Heat Mass Transfer* **2017,** *106*, 473-481.

(16) Agrawal, K. V.; Shimizu, S.; Drahushuk, L. W.; Kilcoyne, D.; Strano, M. S. Observation of Extreme Phase Transition Temperatures of Water Confined inside Isolated Carbon Nanotubes. *Nat. Nanotechnol.* **2017,** *12*, 267-273.

(17) Giovambattista, N.; Rossky, P. J.; Debenedetti, P. G. Phase Transitions Induced by Nanoconfinement in Liquid Water. *Phys. Rev. Lett.* **2009,** *102*, 050603.

(18) Ghosh, S.; Sood, A.; Kumar, N. Carbon Nanotube Flow Sensors. *Science* **2003,** *299*, 1042-1044.

(19) Liu, N.; Jiang, Y.; Zhou, Y.; Xia, F.; Guo, W.; Jiang, L. Two-Way Nanopore Sensing of Sequence-Specific Oligonucleotides and Small-Molecule Targets in Complex Matrices Using Integrated DNA Supersandwich Structures. *Angew. Chem.* **2013,** *125*, 2061-2065.

(20) Sen, Y.-H.; Jain, T.; Aguilar, C. A.; Karnik, R. Enhanced Discrimination of DNA Molecules in Nanofluidic Channels through Multiple Measurements. *Lab Chip* **2012,** *12*, 1094-1101.

(21) Chen, X.; Xu, B.; Liu, L. Nanoscale Fluid Mechanics and Energy Conversion. *Appl. Mech. Rev.* **2014,** *66*.

(22) Siria, A.; Poncharal, P.; Biance, A.-L.; Fulcrand, R.; Blase, X.; Purcell, S. T.; Bocquet, L. Giant Osmotic Energy Conversion Measured in a Single Transmembrane Boron Nitride Nanotube. *Nature* **2013,** *494*, 455-458.

(23) Qiao, Y.; Liu, L.; Chen, X. Pressurized Liquid in Nanopores: A Modified Laplace-Young Equation. *Nano Lett.* **2009,** *9*, 984-988.

(24) Karnik, R.; Fan, R.; Yue, M.; Li, D.; Yang, P.; Majumdar, A. Electrostatic Control of Ions and Molecules in Nanofluidic Transistors. *Nano Lett.* **2005,** *5*, 943-948.

(25) Li, L.; Mo, J.; Li, Z. Nanofluidic Diode for Simple Fluids without Moving Parts. *Phys. Rev. Lett.* **2015,** *115*, 134503.

(26) Mu, J.; Wang, G.; Yan, H.; Li, H.; Wang, X.; Gao, E.; Hou, C.; Pham, A. T. C.; Wu, L.; Zhang, Q.

Molecular-Channel Driven Actuator with Considerations for Multiple Configurations and Color Switching. *Nat. Comm.* **2018,** *9*, 1-10.
(27) Sun, Y.; Rogge, S. M.; Lamaire, A.; Vandenbrande, S.; Wieme, J.; Siviour, C. R.; Van Speybroeck, V.; Tan, J.-C. High-Rate Nanofluidic Energy Absorption in Porous Zeolitic Frameworks. *Nat. Mater.* **2021,** *20*, 1015-1023.
(28) Heiranian, M.; Farimani, A. B.; Aluru, N. R. Water Desalination with a Single-Layer Mos_2 Nanopore. *Nat. Comm.* **2015,** *6*, 1-6.
(29) Kurupath, V. P.; Kannam, S. K.; Hartkamp, R.; Sathian, S. P. Highly Efficient Water Desalination through Hourglass Shaped Carbon Nanopores. *Desalination* **2021,** *505*, 114978.
(30) Noh, Y.; Aluru, N. Phonon-Fluid Coupling Enhanced Water Desalination in Flexible Two-Dimensional Porous Membranes. *Nano Lett.* **2021**.
(31) Wang, C.; Sensale, S.; Pan, Z.; Senapati, S.; Chang, H.-C. Slowing Down DNA Translocation through Solid-State Nanopores by Edge-Field Leakage. *Nat. Comm.* **2021,** *12*, 1-10.
(32) Xu, B.; Qiao, Y.; Chen, X. Mitigating Impact/Blast Energy Via a Novel Nanofluidic Energy Capture Mechanism. *J. Mech. Phys. Solids* **2014,** *62*, 194-208.
(33) Gao, Y.; Li, M.; Zhang, Y.; Lu, W.; Xu, B. Spontaneous Outflow Efficiency of Confined Liquid in Hydrophobic Nanopores. *Proc. Natl. Acad. Sci. U. S. A.* **2020,** *117*, 25246-25253.
(34) Xu, B.; Qiao, Y.; Park, T.; Tak, M.; Zhou, Q.; Chen, X. A Conceptual Thermal Actuation System Driven by Interface Tension of Nanofluids. *Energy Environ. Sci.* **2011,** *4*, 3632-3639.
(35) Kutana, A.; Giapis, K. Atomistic Simulations of Electrowetting in Carbon Nanotubes. *Nano Lett.* **2006,** *6*, 656-661.
(36) Xu, B.; Qiao, Y.; Zhou, Q.; Chen, X. Effect of Electric Field on Liquid Infiltration into Hydrophobic Nanopores. *Langmuir* **2011,** *27*, 6349-6357.
(37) Han, A.; Lu, W.; Punyamurtula, V. K.; Kim, T.; Qiao, Y. Temperature Variation in Liquid Infiltration and Defiltration in a Mcm41. *J. Appl. Phys.* **2009,** *105*, 024309.
(38) Borman, V. D.; Belogorlov, A. A.; Tronin, V. N. J. C.; Physicochemical, S. A.; Aspects, E. Observation of Relaxation of the Metastable State of a Non-Wetting Liquid Dispersed in a Nanoporous Medium. *Colloids Surf. A Physicochem. Eng. Asp.* **2016,** *496*, 63-68.
(39) Guillemot, L.; Biben, T.; Galarneau, A.; Vigier, G.; Charlaix, É. Activated Drying in Hydrophobic Nanopores and the Line Tension of Water. *Proc. Natl. Acad. Sci. U. S. A.* **2012,** *109*, 19557-19562.
(40) Gao, Y.; Li, M.; Zhang, H.; Zhang, Y.; Lu, W.; Xu, B. Anomalous Solid-Like Necking of Confined Water Outflow in Hydrophobic Nanopores. *Matter* **2022,** *5*, 266-280.
(41) Singh, S.; Houston, J.; van Swol, F.; Brinker, C. J. Drying Transition of Confined Water. *Nature* **2006,** *442*, 526-526.
(42) Choudhury, N.; Pettitt, B. M. On the Mechanism of Hydrophobic Association of Nanoscopic Solutes. *J. Am. Chem. Soc.* **2005,** *127*, 3556-3567.
(43) Klesse, G.; Tucker, S. J.; Sansom, M. S. Electric Field Induced Wetting of a Hydrophobic Gate in a Model Nanopore Based on the 5-Ht3 Receptor Channel. *ACS Nano* **2020,** *14*, 10480-10491.
(44) Zhu, F.; Hummer, G. Drying Transition in the Hydrophobic Gate of the Glic Channel Blocks Ion Conduction. *Biophys. J.* **2012,** *103*, 219-227.
(45) Kumar, R.; Schmidt, J.; Skinner, J. Hydrogen Bonding Definitions and Dynamics in Liquid Water. *J. Chem. Phys.* **2007,** *126*, 05B611.
(46) Bonthuis, D. J.; Gekle, S.; Netz, R. R. Profile of the Static Permittivity Tensor of Water at Interfaces: Consequences for Capacitance, Hydration Interaction and Ion Adsorption. *Langmuir* **2012,** *28*, 7679-7694.
(47) Mark, P.; Nilsson, L. Structure and Dynamics of the Tip3p, Spc, and Spc/E Water Models at 298 K. *J. Phys. Chem. A* **2001,** *105*, 9954-9960.
(48) Zhang, Y.; Li, M.; Gao, Y.; Xu, B.; Lu, W. Compressing Liquid Nanofoam Systems: Liquid Infiltration or Nanopore Deformation? *Nanoscale* **2018,** *10*, 18444-18450.
(49) Plimpton, S. Fast Parallel Algorithms for Short-Range Molecular Dynamics. *J. Comput. Phys.* **1995,** *117*, 1-19.
(50) Kamberaj, H.; Low, R.; Neal, M. Time Reversible and Symplectic Integrators for Molecular Dynamics Simulations of Rigid Molecules. *J. Chem. Phys.* **2005,** *122*, 224114.
(51) Berkowitz, M. L.; Bostick, D. L.; Pandit, S. Aqueous Solutions Next to Phospholipid Membrane

Surfaces: Insights from Simulations. *Chem. Rev.* **2006,** *106*, 1527-1539.
(52) Philippsen, A.; Im, W.; Engel, A.; Schirmer, T.; Roux, B.; Müller, D. J. Imaging the Electrostatic Potential of Transmembrane Channels: Atomic Probe Microscopy of Ompf Porin. *Biophys. J.* **2002,** *82*, 1667-1676.
(53) De Luca, S.; Todd, B.; Hansen, J. S.; Daivis, P. J. Molecular Dynamics Study of Nanoconfined Water Flow Driven by Rotating Electric Fields under Realistic Experimental Conditions. *Langmuir* **2014,** *30*, 3095-3109.
(54) Zangi, R.; Mark, A. E. Electrofreezing of Confined Water. *J. Chem. Phys.* **2004,** *120*, 7123-7130.
(55) Ma, M.; Grey, F.; Shen, L.; Urbakh, M.; Wu, S.; Liu, J. Z.; Liu, Y.; Zheng, Q. Water Transport inside Carbon Nanotubes Mediated by Phonon-Induced Oscillating Friction. *Nat. Nanotechnol.* **2015,** *10*, 692-695.
(56) Gelenter, M. D.; Mandala, V. S.; Niesen, M. J.; Sharon, D. A.; Dregni, A. J.; Willard, A. P.; Hong, M. Water Orientation and Dynamics in the Closed and Open Influenza B Virus M2 Proton Channels. *Commun. Biol.* **2021,** *4*, 1-14.

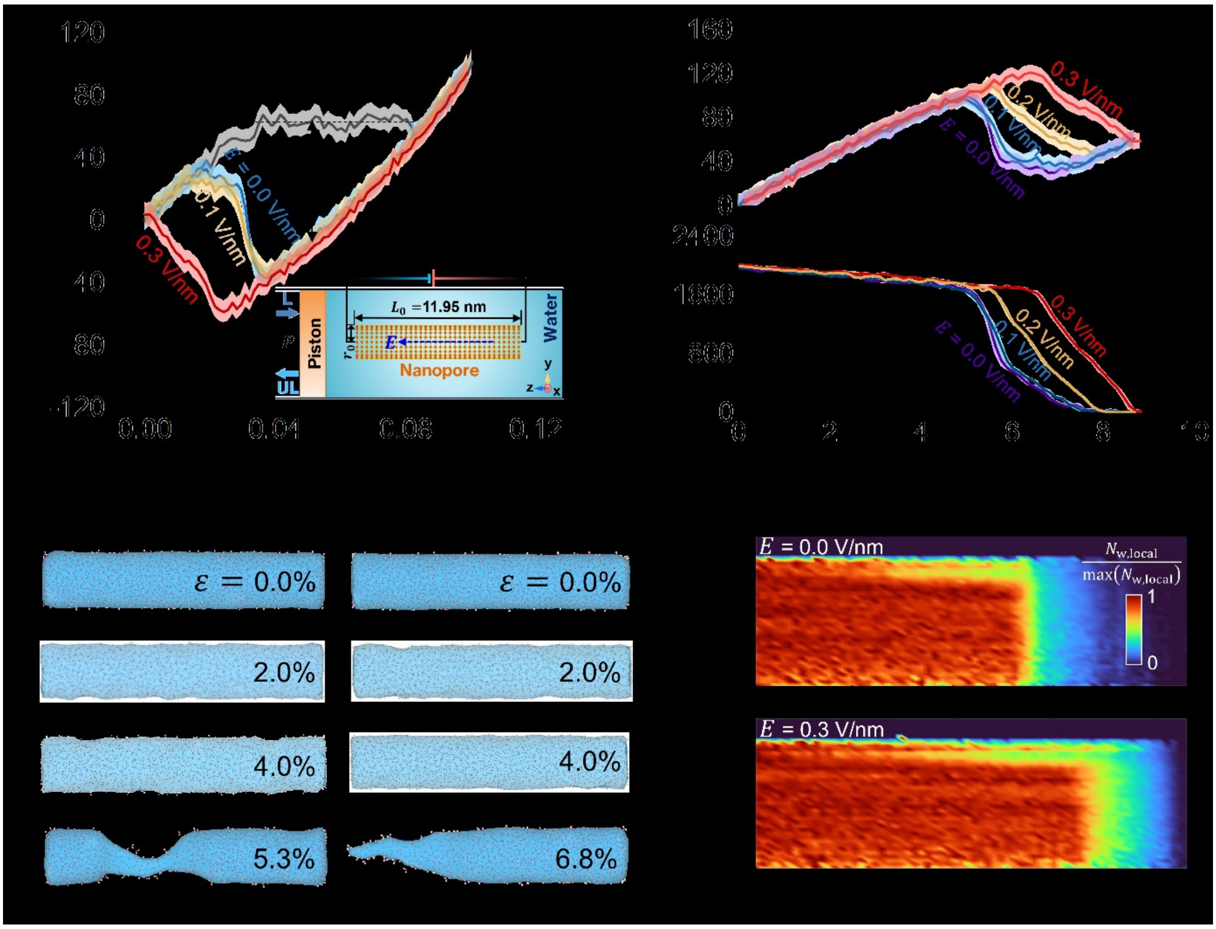

Figure 1. Outflow of intruded liquid from a hydrophobic nanopore under an electric field. (a) Applied pressure P on the piston as a function of the normalized displacement loading $\Delta V/V_0$ during the loading and unloading. The unloading is accompanied by an electric field with strength $E = 0$, 0.1, and 0.3 V/nm. Upon unloading, the pressure difference $(P_{\mathrm{in}} - P)$ reflects the liquid cohesion against the outflow, where P_{in} denotes the infiltration pressure. The confinement radius r_0 is 1.57 nm. Inset: schematic of the atomistic model of the water-hydrophobic nanopore system, which comprises a silica nanotube with a length of L_0 and a variable radius r_0. L and UL stand for loading and unloading, respectively. The electric field is applied in the axial (z-) direction across the nanotube. (b) Nominal stress-strain $(\sigma - \varepsilon)$ relationships during the outflow with different electric field strengths E. The nominal stress σ and strain ε are defined as $(P_{\mathrm{in}} - P)$, and $(\Delta V_{\mathrm{its}}/V_0 - \Delta V/V_0)$, respectively, where ΔV_{its} is the critical volume change that leads to the complete infiltration of the nanotube. (c) Number of confined water molecules N_{w} as a function of ε during the outflow with multiple E values. Uncertainties in (a)-(c) result from averaging the data in the adjacent 15 ps. (d), (e) Atomistic snapshots of confined water cylinders during the outflow with $E = 0$ and 0.3 V/nm. (f), (g) Evolution of the local number of confined water molecules $N_{\mathrm{w,local}}$ with ε at various radial locations r/r_0 and with $E = 0$ and 0.3 V/nm.

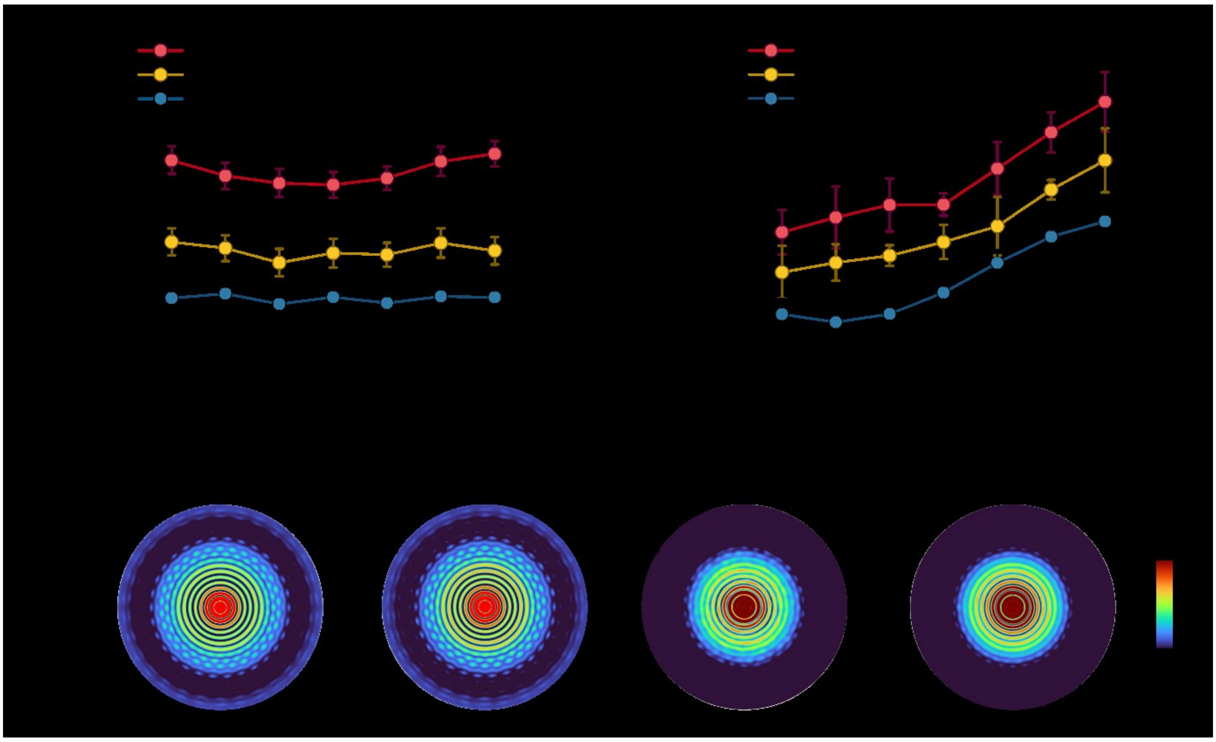

Figure 2. Mechanical characterization of the confined liquid outflow in an electric field. Comparison of (a) elastic moduli Y and (b) ultimate stress F_{TU} of confined water cylinders with different confinement sizes r_0 and electric field strength E. (c) Structural factor $S(\boldsymbol{q})$ of confined water molecules at $\varepsilon = 0$ and 5% and with $E = 0$ and 0.3 V/nm, where $\boldsymbol{q}$ is the scattering vector. The confinement radius r_0 is 1.57 nm.

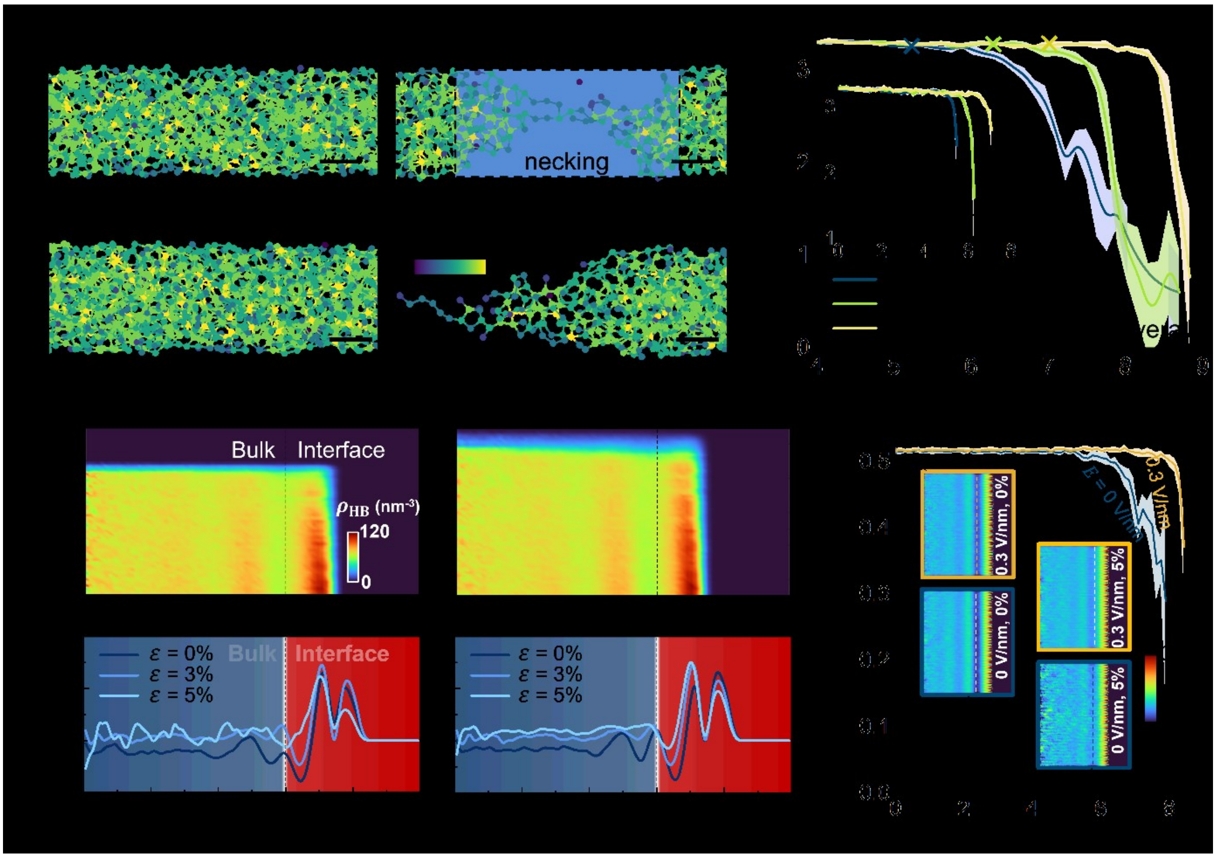

Figure 3. Hydrogen bonding network of the confined water during outflow subject to electric fields. (a) Snapshots of hydrogen-bonding network at different nominal strain ε and with electric field strength $E = 0$ and 0.3 V/nm during the outflow. The confinement radius r_0 is 1.57 nm. All scale bars represent 1 nm. (b) Ensemble average of hydrogen bonds owned by each water molecule $< n_{\mathrm{HB}} >$ as a function of nominal ε with various electric field strengths E. (c), (d) Evolution of the hydrogen bond number density ρ_{HB} with ε at different radial locations r/r_0 and $E = 0$ and 0.3 V/nm. (e), (f) Radial distribution of the axial virial stress σ_{zz} at different ε and with $E = 0$ and 0.3 V/nm. (g) Variation of the H-bond orientation during the outflow with $E = 0$ and 0.3 V/nm, where $\theta_{\mathrm{HB}-z}$ is the angle between the HB and the axial (z-) direction and varies between 0 and 90 degrees. Inset: distributions of $\theta_{\mathrm{HB}-z}$ along radial and axial directions at different ε and with $E = 0$ and 0.3 V/nm.

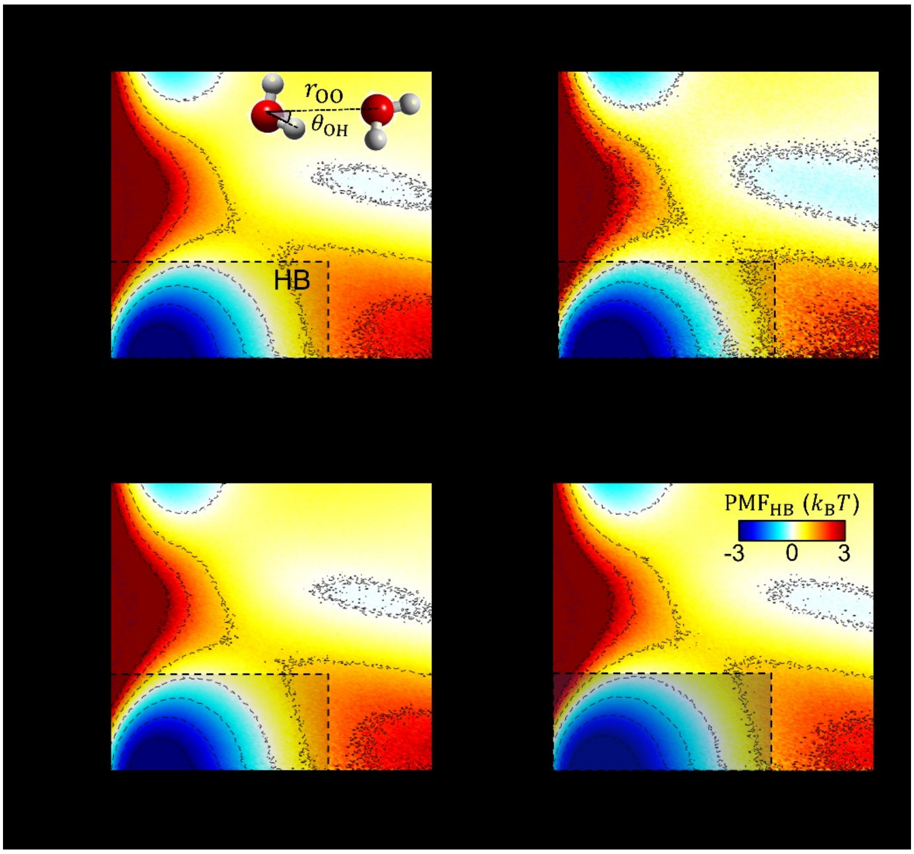

Figure 4. Potential of mean force (PMF) of confined water molecules with (a) $E = 0$ V/nm and $\varepsilon = 0\%$, (b) $E = 0$ V/nm and $\varepsilon = 5\%$, (c) $E = 0.3$ V/nm and $\varepsilon = 0\%$, and (d) $E = 0.3$ V/nm and $\varepsilon = 5\%$, where k_B and T denote the Boltzmann constant and temperature, respectively. Inset of (a): the PMF is based on the molecular separation r_{OO} and pair angle θ_{OH} of each pair of water molecules confined in the nanotube. The confinement radius r_0 is 1.57 nm.

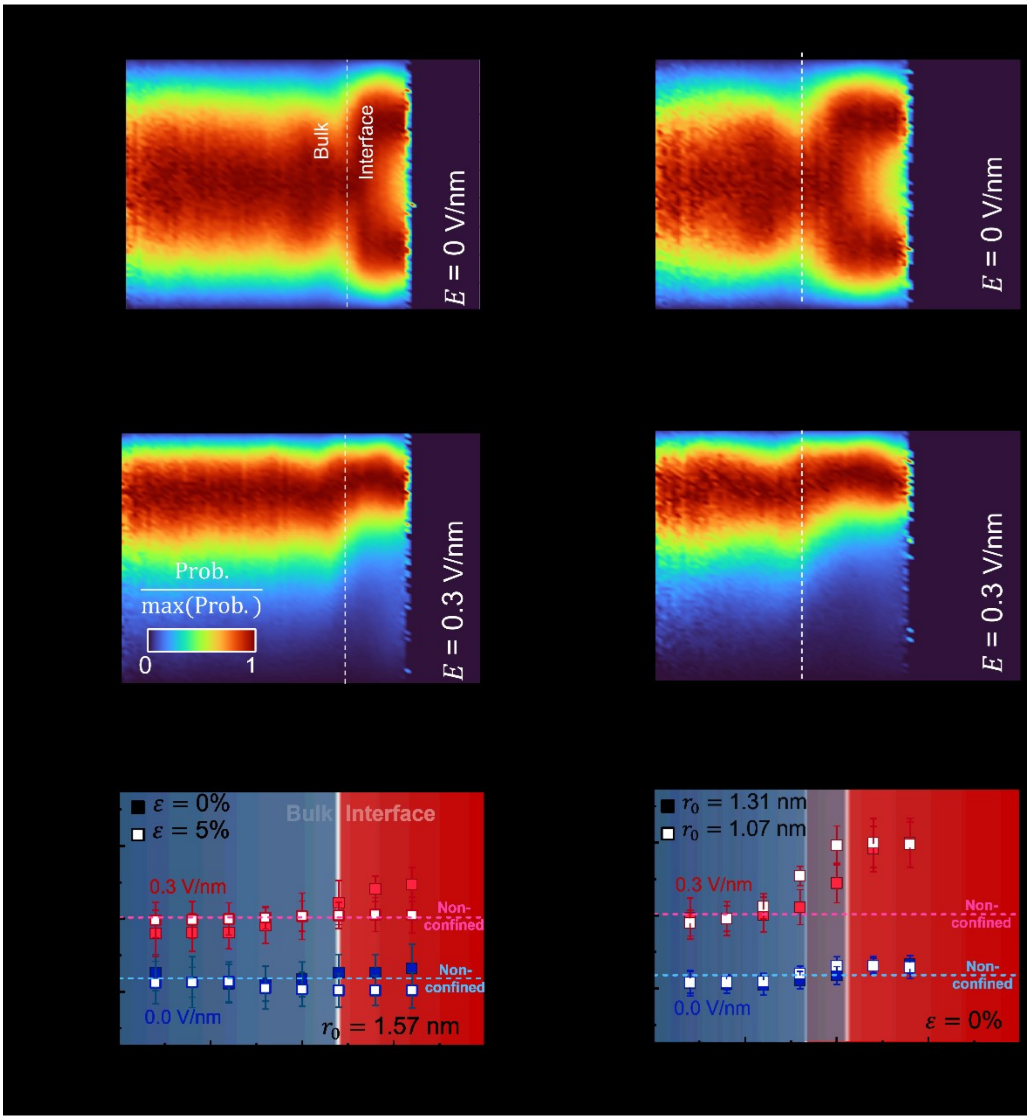

Figure 5. Dipole orientation and rotational dynamics of confined water molecules during the flow subject to an electric field. Probability distribution of the dipole orientation angle $\theta_{\mu-z}$ at different radial locations r/r_0 with (a) $E = 0$ V/nm and (b) $E = 0.3$ V/nm and a confinement size of $r_0 = 1.57$ nm, and (c) $E = 0$ V/nm and (d) $E = 0.3$ V/nm and a confinement size of $r_0 = 1.07$ nm, where $\theta_{\mu-z}$ is the angle between the dipole vector μ and the positive $z-$ direction. Rotational correlation time τ_{rot} at different radial locations r/r_0 (e) with $E = 0$ and 0.3 V/nm, $\varepsilon = 0$ and 5%, a confinement size of $r_0 = 1.57$ nm, and (f) with $E = 0$ and 0.3 V/nm, $\varepsilon = 0$, and confinement pore sizes of $r_0 = 1.31$ and 1.07 nm.

TOC

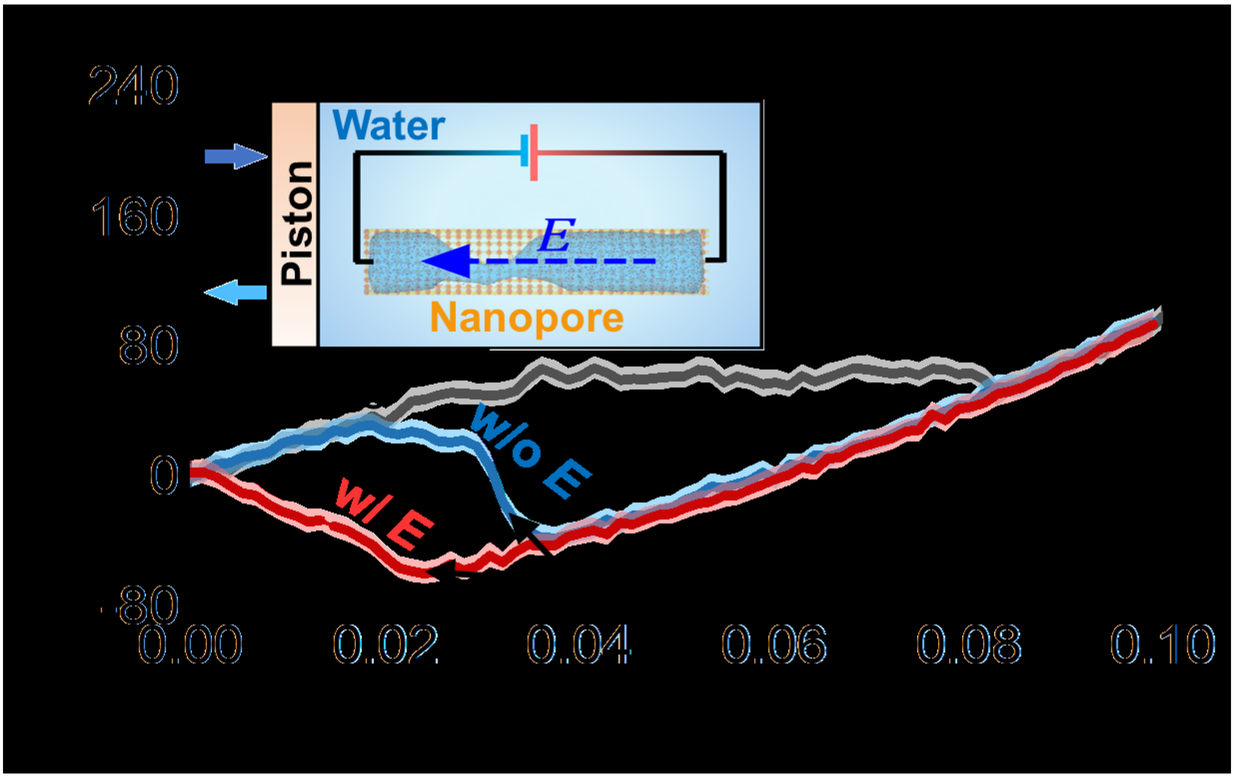
240
160
80
0
-80
0.00
0.02
0.04
0.06
0.08
0.10
Piston
Water
E
Nanopore
w/o E
w/ E